ACS OMEGA

Open Access

http://pubs.acs.org/journal/acsodf

Article

Exploring the Crystal Structure, Thermodynamics, and Molecular Dynamics of $NH(CH_3)_3CuCl_3{\cdot}2H_2O$ Organic–Inorganic Hybrid Perovskite

Changyub Na and Ae Ran Lim*

Cite This: *ACS Omega* 2024, 9, 29789–29796

Read Online

ACCESS | Metrics & More | Article Recommendations | Supporting Information

ABSTRACT: Understanding the physical properties of the organic–inorganic hybrid $NH(CH_3)_3CuCl_3{\cdot}2H_2O$ is necessary for its potential applications. Initially, the monoclinic structure of this crystal was discussed via single-crystal X-ray diffraction. Moreover, the previously unknown phase transition temperature was 350 K, as revealed by differential scanning calorimetry and powder X-ray diffraction. Attributed to ferroelasticity, domain walls were observed between the temperatures T_c (Low) (223 K) and T_c (High) (350 K). Furthermore, changes in chemical shifts for ^1H and ^{13}C indicated alterations in the molecular environment, whereas a notable decrease in line width was attributed to increased molecular motion freedom. Subsequently, spin–lattice relaxation times ($T_{1\rho}$ values) for ^1H and ^{13}C (indicative of energy transfer) were influenced by tumbling motions. The high activation energy barrier for molecular reorientation was associated with the tumbling motion of methyl groups around the triple symmetry axis. These foundational properties guide the development of efficient organic–inorganic hybrids suitable for practical applications.

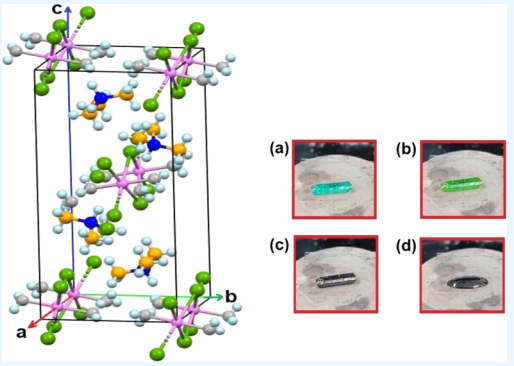

1. INTRODUCTION

Exploring new materials with outstanding electronic, dielectric, and optical properties plays a crucial role in the development of various electronic devices.[1,2] Organic–inorganic hybrid perovskites have garnered considerable attention in optoelectronic devices, such as light-emitting diodes, detectors, photodetectors, and solar cells, owing to their exceptional properties.[3−9] Among them, ABX_3 perovskites undergo phase transitions, exhibiting distinct physical and chemical properties. Numerous studies on organic–inorganic hybrid ABX_3 compounds have yielded meaningful results owing to their broad applicability. In recent efforts to develop advanced materials, researchers have focused on developing materials with ABX_3 stoichiometry, where *A* represents the organic cation (A = NH_3CH_3, $NH_2(CH_3)_2$, $NH(CH_3)_3$, and $N(CH_3)_4$), B denotes the metal cation (B = Co, Zn, Cu, Mn, and Cd), and X denotes the halide anion (X = Cl, Br, and I) for highly efficient photovoltaic applications at a low cost.[1,−22] Crystals with general formulas $ABCl_3{\cdot}2H_2O$ and $ABCl_3$ have garnered considerable attention in recent years due to their specific magnetic properties at low temperatures. Most of these materials undergo multiple structural phase transitions, often related to the reorientation dynamics of the substituted ammonium group. These properties hold promise for applications as temperature and humidity sensors, particularly the characteristic structural phase transition of this material family.[23,24] They correspond to linear chain compounds and behave as very weak one-dimensional Heisenberg ferromagnets. Among them, $NH(CH_3)_3CuCl_3{\cdot}2H_2O$ is an organic–metallic magnetic material with quasi-one-dimensional alternating ferromagnetic and antiferromagnetic Heisenberg chains, and extensive studies have been conducted in this area.[25−29] Being a member of organic–inorganic hybrids, this compound is considered as an ideal model for ferromagnetic–antiferromagnetic chains.

The $NH(CH_3)_3CuCl_3{\cdot}2H_2O$ crystal of the $ABCl_3{\cdot}2H_2O$ type possesses a monoclinic structure with the space group $P2_1/c$. Its lattice constants are a = 7.5066 Å, b = 7.8873 Å, c = 16.758 Å, β = 91.914°, and Z = 4 at 300 K.[27] The crystal structure comprises square-planar $CuCl_2{\cdot}2H_2O$ subunits arranged along the a axis. These hydrogen bonds exhibit intermediate strength and link the $CuCl_2{\cdot}2H_2O$ chains along the b axis. The cations are attracted by very weak bifurcated hydrogen bonds to the $CuCl_2{\cdot}2H_2O$ chains.

According to previous reports, the structure, magnetic susceptibility, and specific heat of the $NH(CH_3)_3CuCl_3{\cdot}2H_2O$ crystal have been documented.[25,28] Moreover, Ritter

Received: April 10, 2024
Revised: June 6, 2024
Accepted: June 10, 2024
Published: June 24, 2024

et al.[27] conducted a study on electron paramagnetic resonance at 4−300 K. Korchak et al.[30] reported a phase transition on the basis of dielectric and dilatometric properties at T_c (low) = 223 K during heating. Furthermore, this phase transition was attributed to the ferroelastic property.

No reports concerning temperatures higher than room temperature with regard to trimethylammonium trichlorocuprate dihydrate ($NH(CH_3)_3CuCl_3{\cdot}2H_2O$) crystals exist. $NH(CH_3)_3CuCl_3{\cdot}2H_2O$ crystals were investigated to determine their crystal structures and identify a new phase transition temperature (T_c). Moreover, the ferroelastic domain walls of the crystal were observed through optical polarizing microscopy. Nuclear magnetic resonance (NMR) chemical shifts as a function of temperature were considered for the structural geometry of the ^1H and ^{13}C atoms. The spin−lattice relaxation time $T_{1\rho}$, representing energy transfer around the ^1H and ^{13}C atoms, was determined as a function of temperature, and their molecular motions and activation energies (E_a) were discussed. These findings provide important information on the structural geometry and energy transfer mechanisms for potential applications.

2. RESULTS AND DISCUSSION

2.1. Crystal Structure. The single-crystal XRD (SXRD) analysis of $NH(CH_3)_3CuCl_3{\cdot}2H_2O$ crystals grown herein was conducted at 250 K, revealing a monoclinic system with space group $P2_1/c$ and lattice constants: a = 7.4979 (8) Å, b = 7.8701 (8) Å, c = 16.740 (2) Å, β = 91.920 (4)°, and Z = 4. These values are consistent with previously reported results.[28] Detailed SXRD data for $NH(CH_3)_3CuCl_3{\cdot}2H_2O$ crystals are listed in Table 1, and the crystal structure and $CuCl_3$ dimer chains at 250 K are depicted in Figure 1a,b (CCDC: 2346144). Bond lengths and angles for each atom are listed in Table 2. Two nonequivalent atoms, i.e., Cu(1) and Cu(2), are observed, coordinated within a square formed by two water molecules and four Cl atoms. These chains comprise edge-sharing $CuCl_4{\cdot}2H_2O$ octahedra running parallel to the a axis, with semicoordinate bonds of Cu−Cl represented by dashed lines. Notably, a correlation exists between the long and short Cu−Cl bonds; the shorter coordinative bond at Cu(2) results in a longer Cu(2)−Cl(1) bond compared to the Cu(1)−Cl(2) bond. Cations are attached through weak bifurcated hydrogen bonds to the $CuCl_4{\cdot}2H_2O$ chains, and additional hydrogen bonds are formed between water molecules of one chain and chlorine atoms of neighboring chains, thereby connecting these chains.

Table 1. Crystal Data and Structure Refinement for $NH(CH_3)_3CuCl_3{\cdot}2H_2O$ at 250 K

chemical formula	$C_3H_{14}NCuCl_3O_2$
weight	266.04
crystal system	monoclinic
space group	$P2_1/c$
T (K)	250
a (Å)	7.4979 (8)
b (Å)	7.8701 (8)
c (Å)	16.740 (2)
β (°)	91.920 (4)
Z	4
V (Å^3)	987.28 (19)
radiation type	Mo−Kα
wavelength (Å)	0.71073
reflections collected	18 490
independent reflections	2464 (R_{int} = 0.0353)
goodness-of-fit on F^2	1.103
final R indices [I > 2sigma(I)]	R_1 = 0.0178, wR_2 = 0.0450
R indices (all data)	R_1 = 0.0204, wR_2 = 0.0460

2.2. Phase Transition Temperature. A differential scanning calorimetry (DSC) thermogram for $NH(CH_3)_3CuCl_3{\cdot}2H_2O$ was obtained at 200−573 K with a heating and cooling rate of 10 °C/min. In the case of heating, the DSC results (Figure 2) indicated a notable deviation from the typical pattern with simultaneous endothermic and exothermic peaks. Specifically, an endothermic peak was detected at 345 K, followed by a prominent exothermic peak at 355 K. Moreover, other exothermic and endothermic peaks were observed at 438−461 K. Enthalpies associated with these four peaks were measured as 17, 189, 118, and 48 kJ/mol, respectively. From these results, $2H_2O$ is decomposed by heating, showing an irreversible process.

To validate the four peaks observed, TGA curves (Figure 2) were obtained while increasing the temperature. The TGA curve indicated thermal stability up to 329 K, corresponding to the partial decomposition temperature (T_d), where a 2% weight loss was observed. However, upon further heating, the molecular weight of $NH(CH_3)_3CuCl_3{\cdot}2H_2O$ crystals abruptly decreased owing to decomposition. The amount of solid residue remaining was calculated on the basis of the molecular weights. The losses of $2H_2O$ and $NH(CH_3)_3Cl{\cdot}2H_2O$ were obtained using eqs 1 and 2.

$$NH(CH_3)_3CuCl_3{\cdot}2H_2O \rightarrow [NH(CH_3)_3CuCl_3(s) + 2H_2O(g)]/NH(CH_3)_3CuCl_3{\cdot}2H_2O = 86.47\% \quad (1)$$

$$NH(CH_3)_3CuCl_3{\cdot}2H_2O \rightarrow [CuCl_2(s) + NH(CH_3)_3Cl{\cdot}2H_2O(g)]/NH(CH_3)_3CuCl_3{\cdot}2H_2O = 50.54\% \quad (2)$$

In $NH(CH_3)_3CuCl_3{\cdot}2H_2O$, mass losses of 14% ($2H_2O$) and 50% ($NH(CH_3)_3Cl{\bullet}2H_2O$) occurred at approximately 406 and 554 K, respectively (Figure 2). At approximately 867 K, a near-complete mass loss is observed. Moreover, changes in the morphology of a single crystal were observed using an optical polarizing microscope as the temperature increased (inset of Figure 2). Initially transparent with a deep green color at 300 K, the crystal gradually transitioned to green and dark brown hues with an increase in temperature, ultimately melting completely at 440 K.

PXRD experiments were conducted at 300, 360, and 440 K. The results obtained in the 2θ measurement range of 8−50° are illustrated in Figure 3. Moreover, a simulated XRD pattern based on the CIF file at 250 K is presented in Figure 3, with peaks observed in this diffractogram indexed using the Mercury program. The PXRD pattern at 300 K, indicated by the blue color, exhibited more similarities than that recorded at 250 K (depicted in black), aligning well with the pattern obtained from the PXRD experiment. However, the PXRD pattern at 360 K (highlighted in red) exhibited fewer

https://doi.org/10.1021/acsomega.4c03446
ACS Omega 2024, 9, 29789−29796

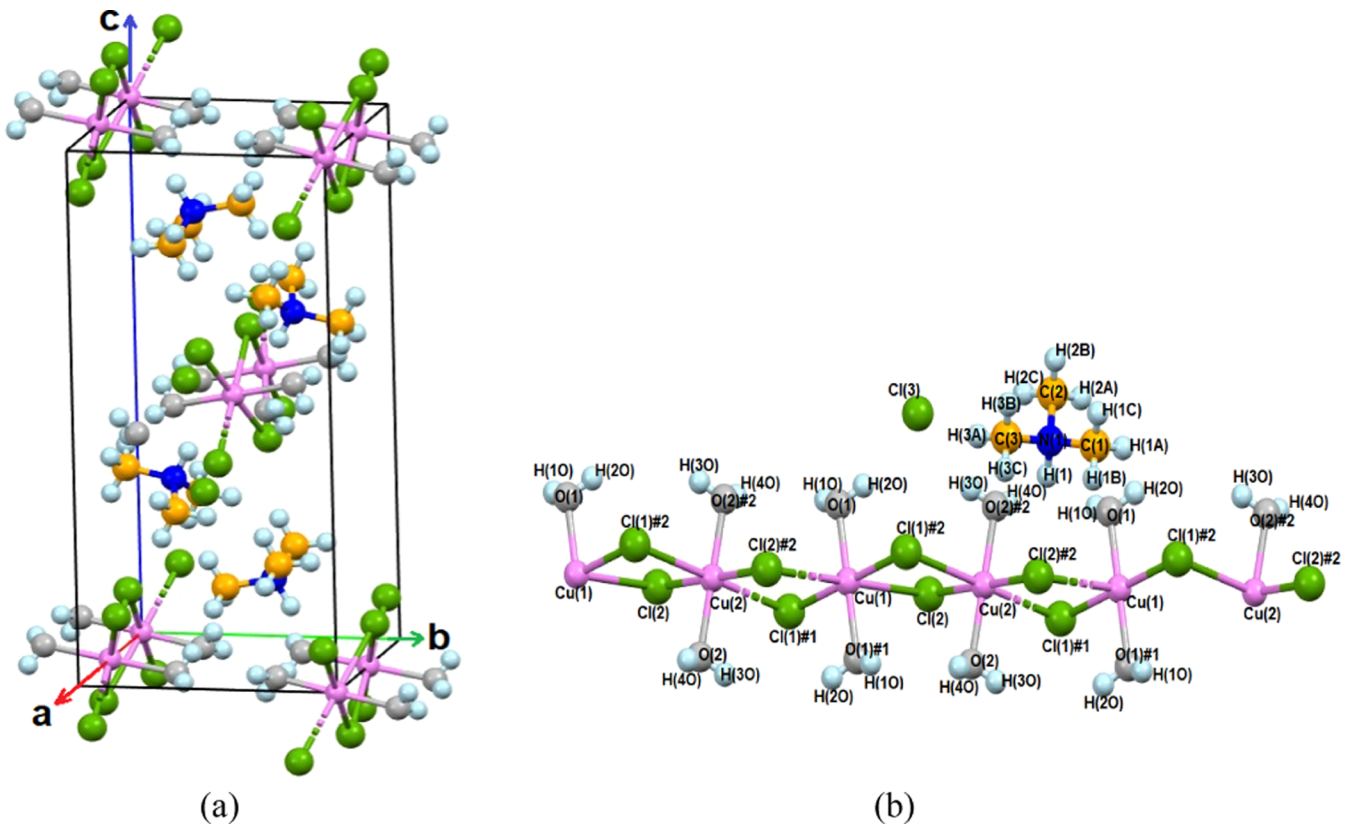

Figure 1. (a) Monoclinic structure of $NH(CH_3)_3CuCl_3{\cdot}2H_2O$ crystal at 250 K (CCDC: 2346144) and (b) $CuCl_3$ dimer chains and $NH(CH_3)_3$ cation along the *a* axis at 250 K. The semicoordinate bonds are denoted by dashed lines (CCDC: 2346144).

differences than that at 300 K, indicating a structural change occurring upon heating at 300−360 K, consistent with a structural transition. This observation confirms the phase transition occurring at 360 K, which falls between 345 and 355 K, according to the DSC results. Finally, the PXRD pattern at 440 K was markedly distinct from those observed at 250, 300, and 360 K, with no discernible crystallinity observed, indicating the onset of melting.

The peaks observed in the DSC curve were effectively supported by the TGA, PXRD, and optical polarizing microscopy experiments. Thus, the new phase transition temperature at high temperatures was T_c (High) = 350 K, and the melting temperature was found to be T_m = 440 K.

2.3. Ferroelastic Domain Walls. Ferroelasticity describes a phenomenon in which materials under external stress exhibit spontaneous strain induced by a phase transition between two equally stable phases, described mainly by lattice orientations. Ferroelastic materials exhibit phase transitions between ferroelastic and paraelastic phases.[31,32] Domain patterns arising from the ferroelastic property of the $NH(CH_3)_3CuCl_3{\cdot}2H_2O$ crystal were investigated using an optical polarizing microscope (Figure 4). The parallel lines in the images represent the twin domain walls, with each photograph captured after approximately 1 min of waiting time for temperature stabilization. The domain walls were observed at a magnification of 200×. At 294 K (Figure 4a), several parallel lines representing the ferroelastic twin domain walls were clearly visible. As the temperature increased, the direction and spacing of the domain walls remained consistent without any notable deviations (Figure 4b−d). This observation supports the assertion that the crystal exhibits ferroelastic properties in the high-temperature phase, as suggested by Korchak et al.[30] At room temperature, the parallel lines of domain walls were distinctly visible. However, as the temperature approached T_C at 350 K, the color of the single crystal darkened, making it challenging to discern the domain walls (Figure 4e−f).

2.4. ^{1}H and ^{13}C Magic Angle Spinning (MAS) NMR Chemical Shifts. NMR chemical shifts and line widths for ^{1}H in the $NH(CH_3)_3CuCl_3{\cdot}2H_2O$ crystal were investigated as a function of temperature, with their temperature dependencies illustrated in Figure 5. As shown in the inset of Figure 5, the ^{1}H NMR spectra for NH, CH_3, and H_2O at 300 K completely overlapped, resulting in one observable signal. Conducting the experiment at a spinning rate of 10 kHz revealed a sideband distance around the ^{1}H signal of 10 kHz (25 ppm), akin to the spinning rate. The main peak and sidebands are indicated by arrows and *, respectively. The change in ^{1}H chemical shift with temperature is presented in Figure 5, with the ^{1}H chemical shift recorded at approximately 6.55 ppm at 300 K. Notably, the chemical shifts exhibited considerable alterations with an increase in temperature, ranging from 6.73 ppm at 250 K to 5.56 ppm at 350 K. Furthermore, the line width decreased sharply near T_c. This result indicates that the coordination geometry around ^{1}H continuously changes with temperature fluctuations, and the molecular motions of ^{1}H become increasingly free near T_C. The decrease in line width near T_c with an increase in temperature is attributed to the internal molecular motion; the molecular motion of ^{1}H became active as the temperature increased.

The ^{13}C NMR chemical shifts of $NH(CH_3)_3CuCl_3{\cdot}2H_2O$ were recorded with an increase in temperature (Figure 6). The adamantane reference signal served as the standard for the ^{13}C

https://doi.org/10.1021/acsomega.4c03446
ACS Omega 2024, 9, 29789−29796

Table 2. Bond Lengths (Å) and Bond Angles (Deg) for $NH(CH_3)_3CuCl_3{\cdot}2H_2O$ at 250 K

bond lengths (Å)		bond angles (°)		bond angles (°)	
Cu(1)−O(1)	1.9708(9)	O(1)−Cu(1)−O(1)#1	180.0	C(2)−N(1)−C(1)	111.73(11)
Cu(1)−O(1)#1	1.9709(9)	O(1)−Cu(1)−Cl(1)#1	91.07(3)	C(2)−N(1)−C(3)	111.29(11)
Cu(1)−Cl(1)#1	2.2792(4)	O(1)#1-Cu(1)−Cl(1)#1	88.93(3)	C(1)−N(1)−C(3)	111.05(11)
Cu(1)−Cl(1)	2.2792(4)	O(1)−Cu(1)−Cl(1)	88.93(3)	C(2)−N(1)−H(1)	107.5
Cu(2)−O(2)	2.0063(9)	O(1)#1-Cu(1)−Cl(1)	91.07(3)	C(1)−N(1)−H(1)	107.5
Cu(2)−O(2)#2	2.0063(9)	Cl(1)#1-Cu(1)−Cl(1)	180.000(14)	C(3)−N(1)−H(1)	107.5
Cu(2)−Cl(2)	2.3083(3)	O(2)−Cu(2)−O(2)#2	180.0	Cu(1)−O(1)−H(1O)	117.2(13)
Cu(2)−Cl(2)#2	2.3083(3)	O(2)−Cu(2)−Cl(2)	89.98(3)	Cu(1)−O(1)−H(2O)	115.0(13)
Cu(2)−Cl(1)	2.7492(4)	O(2)#2-Cu(2)−Cl(2)	90.02(3)	H(1O)-O(1)-H(2O)	106(2)
Cu(2)−Cl(1)#2	2.7492(4)	O(2)−Cu(2)−Cl(2)#2	90.02(3)	Cu(2)−O(2)−H(3O)	112.3(14)
N(1)−C(2)	1.4852(17)	O(2)#2-Cu(2)−Cl(2)#2	89.98(3)	Cu(2)−O(2)−H(4O)	114.0(14)
N(1)−C(1)	1.4870(17)	Cl(2)−Cu(2)−Cl(2)#2	180.0	H(3O)-O(2)-H(4O)	105(2)
N(1)−C(3)	1.4885(17)	O(2)−Cu(2)−Cl(1)	89.81(3)	N(1)−C(1)−H(1A)	109.5
N(1)−H(1)	0.9900	O(2)#2-Cu(2)−Cl(1)	90.19(3)	N(1)−C(1)−H(1B)	109.5
O(1)-H(1O)	0.794(19)	Cl(2)−Cu(2)−Cl(1)	93.577(13)	H(1A)-C(1)-H(1B)	109.5
O(1)-H(2O)	0.83(2)	Cl(2)#2-Cu(2)−Cl(1)	86.423(13)	N(1)−C(1)−H(1C)	109.5
O(2)-H(3O)	0.80(2)	O(2)−Cu(2)−Cl(1)#2	90.19(3)	H(1A)-C(1)-H(1C)	109.5
O(2)-H(4O)	0.77(2)	O(2)#2-Cu(2)−Cl(1)#2	89.81(3)	H(1B)-C(1)-H(1C)	109.5
C(1)-H(1A)	0.9700	Cl(2)−Cu(2)−Cl(1)#2	86.422(13)	N(1)−C(2)−H(2A)	109.5
C(1)-H(1B)	0.9700	Cl(2)#2-Cu(2)−Cl(1)#2	93.578(13)	N(1)−C(2)−H(2B)	109.5
C(1)-H(1C)	0.9700	Cl(1)−Cu(2)−Cl(1)#2	180.000(12)	H(2A)-C(2)-H(2B)	109.5
C(2)-H(2A)	0.9700	Cu(1)−Cl(1)−Cu(2)	95.963(14)	N(1)−C(2)−H(2C)	109.5
C(2)-H(2B)	0.9700			H(2A)-C(2)-H(2C)	109.5
C(2)-H(2C)	0.9700			H(2B)-C(2)-H(2C)	109.5
C(3)-H(3A)	0.9700			N(1)−C(3)−H(3A)	109.5
C(3)-H(3B)	0.9700			N(1)−C(3)−H(3B)	109.5
C(3)-H(3C)	0.9700			H(3A)-C(3)-H(3B)	109.5
				N(1)−C(3)−H(3C)	109.5
				H(3A)-C(3)-H(3C)	109.5
				H(3B)-C(3)-H(3C)	109.5

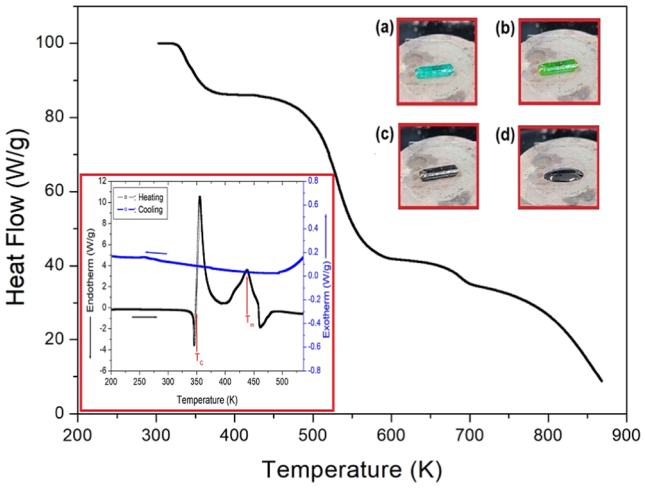

Figure 2. Thermal properties of $NH(CH_3)_3CuCl_3{\cdot}2H_2O$: the thermogravimetry analysis curve of $NH(CH_3)_3CuCl_3{\cdot}2H_2O$ (inset: differential scanning calorimetry curves on heating and cooling and the morphology of a single crystal at (a) 300, (b) 343, (c) 363, and (d) 440 K) (the photos were taken by the author C. Na).

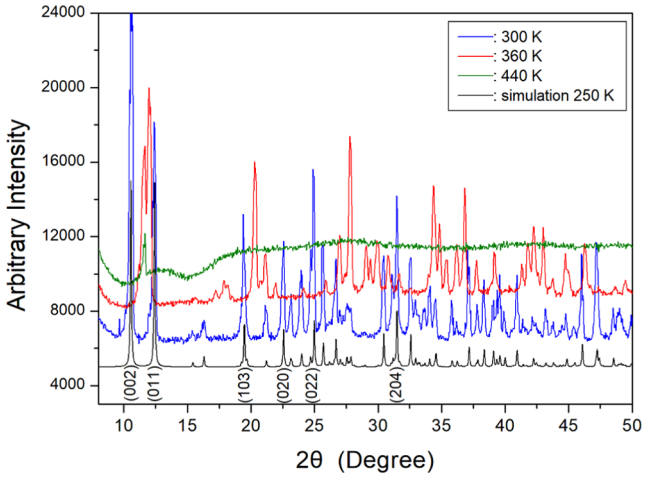

Figure 3. PXRD patterns of $NH(CH_3)_3CuCl_3{\cdot}2H_2O$ at 300, 360, and 440 K. The black color denotes a simulated PXRD pattern at 250 K.

chemical shifts. At 300 K, the ^{13}C resonance signal for the methyl carbon was observed at a chemical shift of 85.60 ppm. The sidebands are denoted as "*x*," with the distance of the sideband around the ^{13}C signal found to be 10 kHz (100 ppm), akin to the spinning rate. Compared with the ^{1}H chemical shifts, the ^{13}C chemical shifts exhibited an abrupt change from 92.68 to 82.02 ppm with an increase in temperature. These alterations in the ^{13}C NMR chemical shifts reflected changes in the coordination geometry around ^{13}C. Furthermore, the line widths experienced a sharp drop from 50 to 2.78 ppm with an increase in temperature. This observation indicates that the molecular motions for ^{13}C exhibited a high degree of freedom for the methyl group.

To acquire the spin−lattice relaxation time ($T_{1\rho}$), the signal intensities of ^{1}H and ^{13}C NMR spectra in $NH(CH_3)_3CuCl_3{\cdot}2H_2O$ were measured while increasing the delay times. The

https://doi.org/10.1021/acsomega.4c03446
ACS Omega 2024, 9, 29789−29796

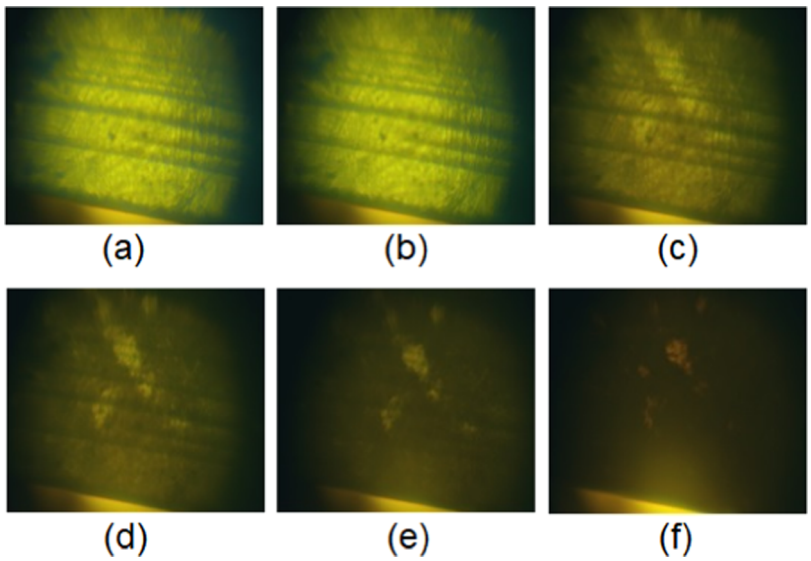

Figure 4. Optical polarizing microscopy images of the $NH(CH_3)_3CuCl_3{\cdot}2H_2O$ single crystal at (a) 294, (b) 313, (c) 323, (d) 330, (e) 333, and (f) 360 K. The visible lines represent the ferroelastic twin domain walls.

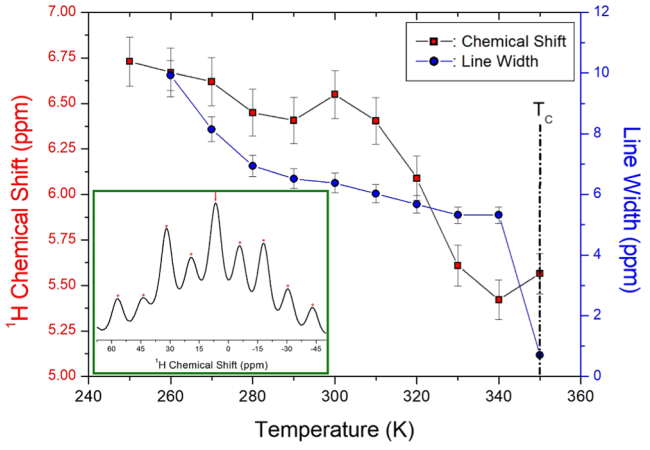

Figure 5. ^{1}H NMR chemical shifts and line widths of $NH(CH_3)_3CuCl_3{\cdot}2H_2O$ as a function of temperature (inset: the ^{1}H NMR spectrum at 300 K; * represents the sidebands).

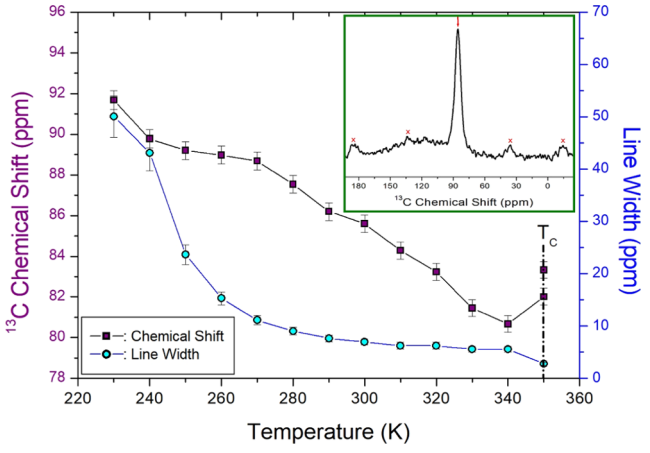

Figure 6. ^{13}C NMR chemical shifts and line widths of $NH(CH_3)_3CuCl_3{\cdot}2H_2O$ as a function of temperature (inset: the ^{13}C NMR spectrum at 300 K; *x* represents the sidebands).

change in intensities and delay times was described using the following equation: $P(t) = P(0)\exp(-t/T_{1\rho})$, where $P(t)$ denotes the intensity of the spectrum at time t and P(0) denotes the intensity at time $t = 0$.[33,34] The intensity changes observed in the ^{1}H and ^{13}C NMR spectra with varying delay times were recorded at a given temperature. Specifically, the ^{1}H NMR spectrum at 300 K was plotted with a delay time ranging from 0.01 to 10 ms (Figure 7a), and the ^{13}C NMR spectrum at 300 K was plotted with a delay time ranging from 0.2 to 7 ms (Figure 7b). On the basis of the slope of the signal intensities of the ^{1}H and ^{13}C indicated by the arrow vs delay times, the ^{1}H and ^{13}C $T_{1\rho}$ values were determined using the aforementioned equation. All decay curves were fitted using a single-exponential function, and the ^{1}H and ^{13}C $T_{1\rho}$ values were obtained on the basis of the slopes of their recovery traces as a function of 1000/temperature (Figure 8). The ^{1}H and ^{13}C $T_{1\rho}$ values were found to be of the order of milliseconds. These values slightly decreased from 240 to 270 K and then increased again with an increase in temperature. At 270 K, the minimum $T_{1\rho}$ values were 0.17 and 0.89 ms for ^{1}H and ^{13}C, respectively. Notably, ^{1}H and ^{13}C $T_{1\rho}$ values rapidly increased near T_C. The short $T_{1\rho}$ values are attributed to the presence of paramagnetic Cu^{2+} ions, with $T_{1\rho}$ being inversely proportional to the square of the magnetic moment of these ions. The $T_{1\rho}$ values decreased owing to the molecular motion of ^{1}H and ^{13}C. These $T_{1\rho}$ values were associated with the correlation time, τ_C, for molecular motion, where the $T_{1\rho}$ value for molecular motion is described by the equation[35−37]

$$1/T_{1\rho} = (\gamma_H\gamma_C\hbar/r^3)^2\{4\tau_C/[1+\omega_1{}^2\tau_C{}^2] + \tau_C/[1+(\omega_H-\omega_C)^2\tau_C{}^2] + 3\tau_C/[1+\omega_C{}^2\tau_C{}^2] + 6\tau_C/[1+(\omega_H+\omega_C)^2\tau_C{}^2] + 6\tau_C/[1+\omega_H{}^2\tau_C{}^2]\} \quad (3)$$

where γ_H and γ_C denote the gyromagnetic ratios for ^{1}H and ^{13}C, respectively, $\hbar$ denotes Planck's constant, r denotes the internuclear distance, ω_H and ω_C denote the Larmor frequencies of ^{1}H and ^{13}C, respectively, and ω_1 denotes the frequency of the spin-lock field. $T_{1\rho}$ was measured with a spin-

https://doi.org/10.1021/acsomega.4c03446
ACS Omega 2024, 9, 29789−29796

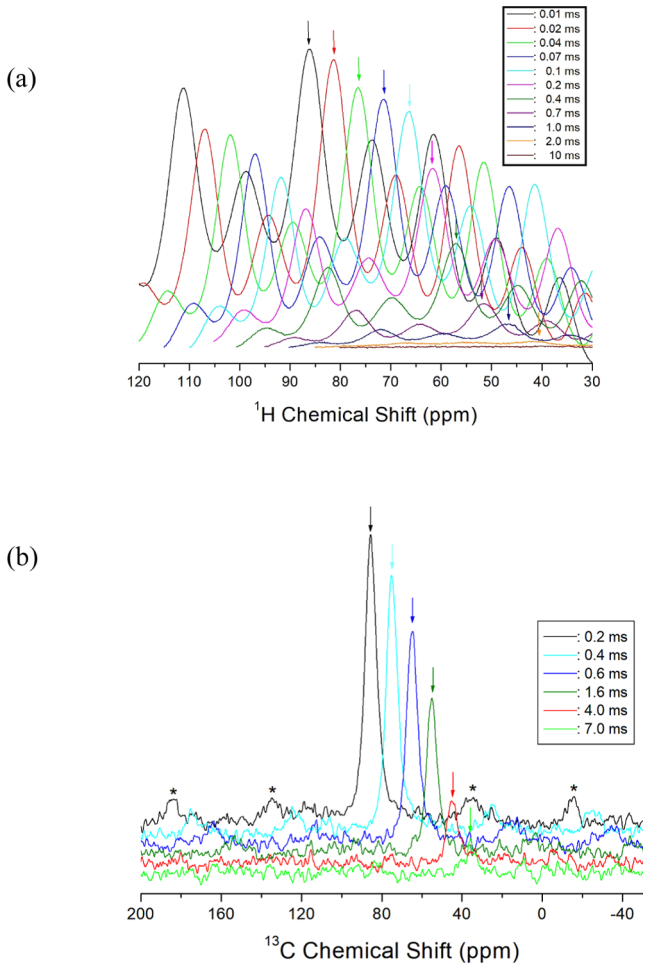

Figure 7. (a) Inversion recovery trace for the ^{1}H NMR spectrum in $NH(CH_3)_3CuCl_3{\cdot}2H_2O$ at 300 K and (b) inversion recovery trace for the ^{13}C NMR spectrum in $NH(CH_3)_3CuCl_3{\cdot}2H_2O$ at 300 K.

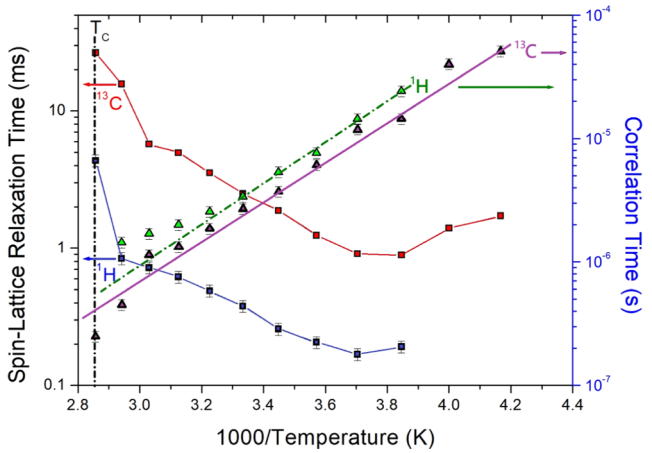

Figure 8. Spin−lattice relaxation times and correlation times for ^{1}H and ^{13}C in $NH(CH_3)_3CuCl_3{\cdot}2H_2O$ as a function of inverse temperature, respectively. The activation energies (E_a) are represented by the slopes of the two solid lines in the plot of correlation time vs 1000/temperature.

lock field of 69.44 kHz using the spin-locking pulse sequence method. $T_{1\rho}$ reached a minimum value when $\omega_1\tau_C = 1$. Therefore, the coefficient in eq 3 can be obtained on the basis of the relationship between $T_{1\rho}$ and ω_1. The correlation time (τ_C) for molecular motion is calculated using the coefficient and $T_{1\rho}$. τ_C as a function of temperature is expressed by the Arrhenius equation: $\tau_C = \tau_o \exp(-E_a/k_BT)$,[38] where E_a denotes the activation energy of motion and k_B denotes the Boltzmann constant. E_a values of 31.39 ± 1.16 and 31.20 ± 3.66 kJ/mol for ^{1}H and ^{13}C, respectively, were obtained from the solid lines shown in Figure 8. Remarkably, the E_a value for ^{1}H was found to be consistent with that for ^{13}C within the error range, indicating that the sources of the interactions between the atoms and ions around the ^{1}H and ^{13}C nuclei are nearly identical. The large E_a values were primarily attributed to the reorientation of the overall $NH(CH_3)_3$ groups.

3. CONCLUSIONS

This study investigated the crystal growth, crystal structure, phase transition temperature, and thermodynamics of the organic−inorganic hybrid $NH(CH_3)_2CuCl_3{\cdot}2H_2O$ crystals. Through SCXRD, the monoclinic structure, bond lengths, and bond angles of these crystals were elucidated. Notably, a previously unknown phase transition temperature of 350 K was revealed using DSC and PXRD results. Ferroelastic properties differed between the previously reported Tc (low) values and the Tc (high) values observed herein. Moreover, changes in the chemical shifts for ^{1}H and ^{13}C, attributed to the local field around the nucleus, indicated alterations in the structural geometry surrounding these nuclei. The sharp decrease in line width was attributed to the high degree of freedom for molecular motion. Furthermore, considerable changes in ^{1}H $T_{1\rho}$ and ^{13}C $T_{1\rho}$ values, representing energy transfer for the ^{1}H and ^{13}C atoms, were observed with varying temperatures, indicating that ^{1}H and ^{13}C are influenced by tumbling motions. The high activation energy barrier for molecular reorientation, inferred from the NMR $T_{1\rho}$ values, was linked to the reorientation of methyl groups around the triple symmetry axis, primarily attributed to the reorientation of the overall $NH(CH_3)_3$ groups below T_c. The results of $CuCl_3$ cations were compared with previously reported data for $CdCl_3$ cations[38] (Table 3). The single-crystal structures exhibited different monoclinic and orthorhombic properties for $CuCl_3$ and $CdCl_3$, respectively, and the T_d temperatures were considerably different at 329 and 522 K. In addition, the difference in ^{1}H and ^{13}C $T_{1\rho}$ for $CuCl_3$ and $CdCl_3$ at 300 K is attributed to the influence of Cu^{2+} paramagnetic ions.

Table 3. Crystal Structure, Lattice Constants (Å), Decomposition Temperature T_d (K), Phase Transition Temperature T_c (K), and Spin−Lattice Relaxation Time $T_{1\rho}$ (*ms*) for $NH(CH_3)_3CuCl_3{\cdot}2H_2O$ and $NH(CH_3)_3CdCl_3$

n	$NH(CH_3)_3CuCl_3{\cdot}2H_2O$	$NH(CH_3)_3CdCl_3$
structure	monoclinic	orthorhombic
space group	$P2_1/c$	*Pnma*
lattice constants		
a (Å)	7.4979	14.5088
b (Å)	7.8701	6.7108
c (Å)	16.740	8.9901
β (°)	91.920	
Z	4	4
T_d	329	522
T_C	350	345, 376, 452
^{1}H $T_{1\rho}$	0.37	110−150
^{13}C $T_{1\rho}$	2.50	225

https://doi.org/10.1021/acsomega.4c03446
ACS Omega 2024, 9, 29789−29796

Physicochemical properties considerably varied owing to the difference in the characteristics of the cations. This comprehensive study provides valuable insights into the fundamental properties of organic−inorganic hybrid materials, facilitating their practical applications.

4. EXPERIMENTAL METHODS

4.1. Crystal Growth. To grow $NH(CH_3)_3CuCl_3{\cdot}2H_2O$ single crystals, $NH(CH_3)_3Cl$ (Aldrich, 98%) and $CuCl_2{\cdot}2H_2O$ (Aldrich, 95%) were prepared at a 1:1 molar ratio and dissolved in distilled water. It was stirred and heated to create a completely saturated solution, which was then filtered once through a filter paper. A single, deep green prismatic crystal ($10 \times 2 \times 2$ mm^3), elongated along the b axis, was obtained via slow evaporation at 300 K over several weeks. To prevent moisture-induced degradation, the crystals were stored in a desiccator.

4.2. Characterization. The structure and lattice parameters of $NH(CH_3)_3CuCl_3{\cdot}2H_2O$ crystals were determined through SCXRD at the Seoul Western Center of the Korea Basic Science Institute (KBSI). The crystal block was mounted on a diffractometer (Bruker D8 Venture PHOTON III M14) equipped with a graphite-monochromated Mo−Kα (λ = 0.71073 Å) radiation source. Data were collected and integrated using SMART APEX3 and SAINT. Direct methods were used to solve the structure, followed by refinement via full-matrix least-squares on F2 using SHELXTL.[39] Additionally, powder X-ray diffraction (PXRD) patterns of $NH(CH_3)_3CuCl_3{\cdot}2H_2O$ were obtained using an XRD system with the same Mo−Kα source used in SCXRD.

DSC measurements were conducted using a DSC instrument (TA Instruments, DSC 25) with a heating rate of 10 °C/min within the temperature range of 200 to 573 K under a flow of nitrogen gas. The sample quantity utilized in the DSC experiment was 4.4 mg. Additionally, thermogravimetric analysis (TGA) was performed at a heating rate of 10 °C/min within the temperature range of 300 to 873 K under a nitrogen atmosphere. The powder sample employed in the TGA experiment weighed 7.52 mg. The morphologies of the single crystal were observed in response to temperature variations, and the ferroelastic domain walls were examined using an optical polarizing microscope equipped with a hot stage (Linkam THMS 600) for temperature control.

The MAS NMR chemical shifts and spin−lattice relaxation time $T_{1\rho}$ of $NH(CH_3)_3CuCl_3{\cdot}2H_2O$ crystals were determined using a solid-state NMR spectrometer (Bruker, AVANCE III+) at the Western Seoul Center of the KBSI. The Larmor frequency for the ^{1}H NMR experiment was set at 400.13 MHz and adjusted to 100.61 MHz for the ^{13}C NMR experiment. Samples were placed in cylindrical zirconia rotors and spun at 10 kHz for MAS NMR measurements to minimize spinning sidebands. Chemical shifts were referenced to adamantane and tetramethylsilane for ^{1}H and ^{13}C, respectively, serving as standard materials to ensure accuracy. One-dimensional NMR spectra for ^{1}H and ^{13}C were acquired with delay times ranging from 2 to 20 s. ^{1}H $T_{1\rho}$ values were determined using a $\pi/2-\tau$ spin-lock pulse with a duration of τ, employing a $\pi/2$ pulse width of 3.65−4 μs. Similarly, ^{13}C $T_{1\rho}$ values were obtained by varying the duration of a ^{13}C spin-locking pulse post the cross-polarization preparation period.

ASSOCIATED CONTENT

Supporting Information

The Supporting Information is available free of charge at https://pubs.acs.org/doi/10.1021/acsomega.4c03446.

$NH(CH_3)_3CuCl_3{\cdot}2H_2O$ 250 K (CIF)

Accession Codes

Data sets generated and/or analyzed during the current study are available in the CCDC (2346144).

AUTHOR INFORMATION

Corresponding Author

Ae Ran Lim − *Graduate School of Carbon Convergence Engineering, Jeonju University, Jeonju 55069, South Korea; Department of Science Education, Jeonju University, Jeonju 55069, South Korea;* orcid.org/0000-0002-5242-9189; Phone: +82-(0)63-220-2514; Email: aeranlim@hanmail.net, arlim@jj.ac.kr; Fax: +82-(0)63-220-2053

Author

Changyub Na − *Graduate School of Carbon Convergence Engineering, Jeonju University, Jeonju 55069, South Korea*

Complete contact information is available at: https://pubs.acs.org/10.1021/acsomega.4c03446

Notes

The authors declare no competing financial interest.

ACKNOWLEDGMENTS

This study was supported by the National Research Foundation of Korea (NRF), funded by the Korean government (MSIT) (2023R1A2C2006333), and the Basic Science Research Program of the National Research Foundation of Korea (NRF), funded by the Ministry of Education, Science, and Technology (2016R1A6A1A03012069).

REFERENCES

(1) Senanayak, S. P.; Abdi-Jalebi, M.; Kamboj, V. S.; Carey, R.; Shivanna, R.; Tian, T.; Schweicher, G.; Wang, J.; Giesbrecht, N.; Nuzzo, D. D.; Beere, H. E.; Docampo, P.; Ritchie, D. A.; Fairen-Jimenez, D.; Friend, R. H.; Sirringhaus, H. A general approach for hysteresis-free, operationally stable metal halide perovskite field-effect transistors. *Sci. Adv.* **2020**, *6*, No. eaaz4948, DOI: 10.1126/sciadv.aaz4948.

(2) Kalthoum, R.; Bechir, M. B.; Rhaiem, A. B.; Gargouri, M. $MCdCl_3$ (M = CH_3NH_3, $(CH_3)_2NH_2$): New hybrid perovskites with large dielectric constants for field-effect transistors. *Phys. Status Solidi A* **2021**, *218*, No. 2100485, DOI: 10.1002/pssa.202100485.

(3) Ji, C.; Wang, P.; Wu, Z.; Sun, Z.; Li, L.; Zhang, J.; Hu, W.; Hong, M.; Luo, J. Inch-size single crystal of a lead-free organic−inorganic hybrid perovskite for high-performance photodetector. *Adv. Funct. Mater.* **2018**, *28*, No. 1705467, DOI: 10.1002/adfm.201705467.

(4) Liao, Q.; Jin, X.; Fu, H. Tunable halide perovskites for miniaturized solid-state laser applications. *Adv. Opt. Mater.* **2019**, *7*, No. 1900099, DOI: 10.1002/adom.201900099.

(5) Zhang, Q.; Ha, S. T.; Liu, X.; Sum, T. C.; Xiong, Q. Room-temperature near-infrared high-Q perovskite whispering-gallery planar nanolasers. *Nano Lett.* **2014**, *14*, 5995.

(6) Geffroy, C.; Grana, E.; Bessho, T.; Almosni, S.; Tang, Z.; Sharma, A.; Kinoshita, T.; Awai, F.; Cloutet, E.; Toupance, T.; Segawa, H.; Hadziioannou, G. p-Doping of a hole transport material via a poly(ionic liquid) for over 20% efficiency and hysteresis-free perovskite solar cells. *ACS Appl. Energy Mater.* **2020**, *3*, 1393.

(7) Yakunin, S.; Dirin, D. N.; Shynkarenko, Y.; Morad, V.; Cherniukh, I.; Nazarenko, O.; Kreil, D.; Nauser, T.; Kovalenko, M.

V. Detection of gamma photons using solution-grown single crystals of hybrid lead halide perovskites. *Nat. Photonics* **2016**, *10*, 585.
(8) Bao, C.; Yang, J.; Bai, S.; Xu, W.; Yan, Z.; Xu, Q.; Liu, J.; Zhang, W.; Gao, F. High performance and stable all-inorganic metal halide perovskite-based photodetectors for optical communication applications. *Adv. Mater.* **2018**, *30*, No. 1803422, DOI: 10.1002/adma.201803422.
(9) Dou, L.; Yang, Y. M.; You, J.; Hong, Z.; Chang, W. H.; Li, G.; Yang, Y. Solution-processed hybrid perovskite photodetectors with high detectivity. *Nat. Commun.* **2014**, *5*, No. 5404, DOI: 10.1038/ncomms6404.
(10) Kalthoum, R.; Bechir, M. B.; Rhaiem, A. B.; Dhaou, M. H. Optical properties of new organic-inorganic hybrid perovskites $(CH_3)_2NH_2CdCl_3$ and $CH_3NH_3CdCl_3$ for solar cell applications. *Opt. Mater.* **2022**, *125*, No. 112084, DOI: 10.1016/j.optmat.2022.112084.
(11) Jellali, H.; Msalmi, R.; Smaoui, H.; Elleuch, S.; Tozri, A.; Roisnel, T.; Mosconi, E.; Althubiti, N. A.; Naïli, H. Zn^{2+} and Cu^{2+} doping of one-dimensional lead-free hybrid perovskite ABX_3 for white light emission and green solar cell applications. *Mater. Res. Bull.* **2022**, *151*, No. 111819.
(12) Kapustyanyk, V. B.; Korchak, Y. M.; Bazhan, V. V.; Éliyashevskii, Y. I. Temperature change in the electronic spectra of an $NH_2(CH_3)_2CuCl_3$ crystal in phase transitions. *J. Appl. Spectrosc.* **2002**, *69*, 406.
(13) Willett, R. D. Crystal structure and optical properties of $(CH_3)_2NH_2CuCl_3$. *J. Chem. Phys.* **1966**, *44*, 39.
(14) Hurley, M.; Gerstein, B. C. Low temperature heat capacities of one dimensional systems: Dimethylammonium trichlorocuprate(II) and tetramethylammonium trichloronickelate(II). *J. Chem. Phys.* **1973**, *59*, 6667.
(15) Stone, M. B.; Tian, W.; Granroth, G. E.; Lumsden, M. D.; Chung, J.-H.; Mandrus, D. G.; Nagler, S. E. Spin dynamics of the low-dimensional magnet $(CH_3)_2NH_2CuCl_3$. *Phys. B: Condens. Matter* **2006**, *385*−*386*, 438.
(16) Losee, D. B.; McElearney, J. N.; Shankle, G. E.; Carlin, R. L.; Cresswell, P. J.; Robinson, W. T. An anisotropic low-dimensional Ising system, $[(CH_3)_3NH]CoCl_3{\cdot}2H_2O$: Its structure and canted antiferromagnetic behavior. *Phys. Rev. B* **1973**, *8*, 2185.
(17) Kapustianik, V.; Batiuk, A.; Dacko, S. Dielectric properties and absorption spectra of trimethylammonium trichlorcobaltate dihydrate single crystals. *Phys. Status Solidi A* **2004**, *241*, 1939.
(18) Chen, L. M.; Tao, W.; Zhao, Z. Y.; Li, Q. J.; Ke, W. P.; Wang, X. M.; Liu, X. G.; Fan, C.; Sun, X. F. Growth of $(CH_3)_2NH_2CuCl_3$ single crystals using evaporation method with different temperatures and solvents. *J. Cryst. Growth* **2010**, *312*, 3243.
(19) Yoshida, Y.; Wada, O.; Inagaki, Y.; Asano, T.; Takeo, K.; Kawae, T.; Takeda, K.; Ajiro, Y. Specific heat study of novel spin-gapped system: $(CH_3)_2NH_2CuCl_3$. *J. Phys. Soc. Jpn.* **2005**, *74*, 2917.
(20) Chen, L. M.; Wang, X. M.; Ke, W. P.; Zhao, Z. Y.; Liu, X. G.; Fan, C.; Li, Q. J.; Zhao, X.; Sun, X. F. Heat transport of the quasi-one-dimensional alternating spin chain material $(CH_3)_2NH_2CuCl_3$. *Phys. Rev. B* **2011**, *84*, No. 134429.
(21) Inagaki, Y.; Kobayashi, A.; Asano, T.; Sakon, T.; Kitagawa, H.; Motokawa, M.; Ajiro, Y. Novel alternating dimer chain system $(CH_3)_2NH_2CuCl_3$ studied by X-ray structural analyses and magnetization process. *J. Phys. Soc. Jpn.* **2005**, *74*, 2683.
(22) Willett, R. D.; Twamley, B.; Montfooij, W.; Granroth, G. E.; Nagler, S. E.; Hall, D. W.; Park, J.-H.; Watson, B. C.; Meisel, M. W.; Talham, D. R. Dimethylammonium trichlorocuprate(II): structural transition, low-temperature crystal structure, and unusual two-magnetic chain structure dictated by nonbonding chloride−chloride contacts. *Inorg. Chem.* **2006**, *45*, 7689−7697, DOI: 10.1021/ic060654u.
(23) Kchaou, H.; Karoui, K.; Bulou, A.; Rhaiem, A. B. Raman spectroscopy studies of temperature induced phase transitions in$[N(CH_3)_3H]CdCl_3$ and DFT (B3LYP) calculations. *Phys. E* **2017**, *88*, 50 DOI: 10.1016/j.physe.2016.11.019.
(24) Karoui, A.; Ben Rhaiem, A.; Jomni, F.; Moneger, J. L.; Bulou, A.; Guidara, K. Characterization of phase transitions of $[N(CH_3)_4]_2ZnCl_2Br_2$ crystals. *J. Mol. Struct.* **2013**, *1048*, 287.
(25) Losee, D. B.; McElearney, J. N.; Siegel, A.; Carlin, R. L.; Khan, A. A.; Roux, J. P.; James, W. J. Structural and magnetic properties of $[(CH_3)_3NH]CuCl_3{\cdot}2H_2O$. *Phys. Rev. B* **1972**, *6*, 4342.
(26) Algra, H. A.; De Jongh, L. J.; Huiskamp, W. J.; Carlin, R. L. Magnetic behavior of $[(CH_3)_3NH]CuCl_3{\cdot}2H_2O$. Evidence for lattice-dimensionality crossovers in a quasi-one-dimensional ferromagnet. *Physica B+C* **1977**, *92*, 187−200, DOI: 10.1016/0378-4363(77)90019-5.
(27) Ritter, M. B.; Drumheller, J. E.; Kite, T. M.; Snively, L. O.; Emerson, K. Electron paramagnetic resonance of $[(CH_3)_3NH]CuCl_3{\cdot}2H_2O$. *Phys. Rev. B* **1983**, *28*, No. 4949, DOI: 10.1103/PhysRevB.28.4949.
(28) Pabst, I.; Bats, J. W. Refinement of trimethylammonium trichlorocuprate(II) dihydrate, $[NH(CH_3)_3][CuCl_3]{\cdot}2H_2O$. *Acta Crystallogr.* **1985**, *C41*, No. 1297, DOI: 10.1107/S010827018500751X.
(29) Miao, L.-P.; Ding, N.; Wang, N.; Shi, C.; Ye, H.-Y.; Li, L.; Yao, Y.-F.; Dong, S.; Zhang, Y. Direct observation of geometric and sliding ferroelectricity in an amphidynamic crystal. *Nat. Mater.* **2022**, *21*, 1158.
(30) Lun, M.-M.; Luo, J.-Q.; Zhang, Z.-X.; Li, J.; Xie, L.-Y.; Lu, H.-F.; Zhang, Y.; Fu, D.-W. Piezoelectric self-power supply driven by ferroelastic host-guest supramolecule with considerable electromechanical conversion capability. *Chem. Eng. J.* **2023**, *475*, No. 145969, DOI: 10.1016/j.cej.2023.145969.
(31) Salje, E. K. H. Ferroelastic materials. *Annu. Rev. Mater. Res.* **2012**, *42*, 265.
(32) Korchak, Y.; Kapustianik, V.; Batiuk, A.; Girnyk, I.; Czapla, Z.; Dacko, S. Dielectric and dilatometric properties of $NH(CH_3)_3CuCl_3{\cdot}2H_2O$ low dimensional ferroics. *Acta Phys. Pol., A* **2004**, *106*, 39.
(33) Lim, A. R.; Kim, S. H. Processing on crystal growth, structure, thermal property, and nuclear magnetic resonance of organic−inorganic hybrid perovskite type $[NH_3(CH_2)_6NH_3]ZnCl_4$ crystal. *RSC Adv.* **2023**, *13*, 31027.
(34) Kim, S. H.; Joo, Y. L.; Lim, A. R. Analysis of the structure, thermal, and molecular dynamics of organic−inorganic hybrid crystal at phases IV, III, II, and I: $[NH_2(CH_3)_2]_2CdBr_4$. *ACS Omega* **2023**, *8*, 34180.
(35) Abragam, A. *The Principles of Nuclear Magnetism*; Oxford Univ. press, 1961.
(36) Harris, R. K. *Nuclear Magnetic Resonance Spectroscopy*; Pitman Pub., UK, 1983.
(37) Koenig, J. L. *Spectroscopy of Polymers*; Elsevier: New York, 1999.
(38) Lim, A. R. Investigation of the structure, phase transitions, molecular dynamics, and ferroelasticity of organic-inorganic hybrid $NH(CH_3)_3CdCl_3$ crystals. *RSC Adv.* **2023**, *13*, 18538.
(39) *SHELXTL v 6.10*; Bruker AXS, Inc.: Madison, Wisconsin, USA, 2000.

https://doi.org/10.1021/acsomega.4c03446
ACS Omega 2024, 9, 29789−29796